



A coupling approach of discretized peridynamics with finite element method

Wenyang Liu^a, Jung-Wuk Hong^{a,b,*}

^a Department of Civil and Environmental Engineering, Michigan State University, East Lansing, MI 48824, United States

^b Department of Civil and Environmental Engineering, Korea Advanced Institute of Science and Technology, Daejeon 305-701, Republic of Korea

ARTICLE INFO

Article history:

Received 18 January 2012

Received in revised form 28 June 2012

Accepted 2 July 2012

Available online 25 July 2012

Keywords:

Peridynamics

Finite element method

Fracture

ABSTRACT

Peridynamics is a reformulated theory of classical continuum mechanics, and it remains valid at discontinuities. However, peridynamics compared to the finite element method (FEM) is computationally expensive. In the present paper, an approach to couple the discretized peridynamics and FEM is proposed to take advantage of the generality of peridynamics and the computational efficiency of FEM. Peridynamic and finite element subregions are coupled by means of interface elements, and two types of coupling schemes are introduced. Numerical examples are investigated under quasi-static conditions. The displacement of a one-dimensional bar using the coupling approach is compared with the classical (local) solution. Deformations of a three-dimensional bar and Poisson effect at interfaces of the coupling model are studied. The capability of the coupling approach for problems involving damage is demonstrated by modeling mixed mode fracture in a double-edge-notched specimen. Numerical predictions of crack paths are compared with the experiment by Nooru-Mohamed et al. (1993) [19].

© 2012 Elsevier B.V. All rights reserved.

1. Introduction

Fracture is one of major concerns in the engineering field for a long time, and people have made substantial efforts in order to understand material failures and alleviate potential dangers. Inglis and Griffith made contributions to the early development of fracture analyses, and Irwin extended the Griffith approach by developing the energy release rate [1]. Fracture mechanics provides a more reliable methodology for engineering designs than the traditional strength based approach. However, classical fracture mechanics has its limitations. For example, a pre-existing crack needs to be defined, and the fracture process zone is required to be small compared to geometrical dimensions [2,3].

In order to model crack growth and material damage, various numerical methods have been studied. The cohesive crack model addresses relationships between the crack opening displacement and the cohesive tractions resisting the separation of cracks [4–6]. The cohesive zone models have been incorporated into finite element (FE) models using interface elements and contact surfaces. The partition of unity finite element method (PUFEM) was presented by Melenk and Babuska [7]. Belytschko and collaborators [8,9] investigated the partition of unity principle for simulations of fracture problems and developed the extended finite element method (XFEM). The XFEM allows the discontinuity not

constrained to element boundaries, and it can model the discontinuity without remeshing [10]. Mariani and Perego [11] presented a method for the simulation of quasi-static cohesive crack propagation using the XFEM for quasi-brittle materials. Cox [10] proposed enrichment functions to represent the discontinuity using an analytical investigation of the cohesive crack problem. Considering the minimization of the total energy of the global system, Meschke and Dumstorff [12] proposed a variational form of XFEM for the propagation of cohesive and cohesionless cracks in quasi-brittle solids. Meshfree and particle methods [13] demonstrate capability for numerical simulations of material failures. Molecular dynamics, for example, is capable of investigating nonlinearities in the vicinity of cracks, the bond breaking between atoms, and the formation of extended defects [14–16]. Research on coupling finite element methods and meshless methods [17,18] has also been conducted.

A great deal of research effort has been made to study many fracture problems. One common benchmark problem characterized by the mixed mode fracture is the test of a double-edge-notched concrete specimen conducted by Nooru-Mohamed et al. [19]. The test of Nooru-Mohamed was adopted by De Borst [20] in the discussion of computational modeling of concrete fracture. For the analyses, the finite element smeared-crack approach with the gradient Rankine plasticity model, Cruch-Crack model, and Ottosen's model has been used for numerical studies of Nooru-Mohamed's experiment by Di Prisco et al. [21]. A comparative study of three-dimensional constitutive models for the double-edge-notched test was performed by Pivonka et al. [22]. Gasser and Holzapfel [23] employed the cohesive crack model with the PUFEM for the numerical modeling of the test. The XFEM was

* Corresponding author at: Department of Civil and Environmental Engineering, Korea Advanced Institute of Science and Technology, 291 Daehak-ro, Yuseong-gu, Daejeon 305-701, Republic of Korea. Tel.: +82 42 350 3616.

E-mail address: jwhong@alum.mit.edu (J.-W. Hong).

utilized by Cox [10], Meschke and Dumstorff [12], and Unger et al. [24] for the simulations. An adaptive mesh refinement technique applied to a nonlocal version of anisotropic damage model was employed by Patzák and Jirásek [25]. Réthoré et al. [26] used a hybrid analytical and XFEM to study the propagation of curved cracks in the double-edge-notched concrete specimen.

As a reformulated theory of continuum mechanics, peridynamics eliminates the spatial derivatives, and it is valid regardless of discontinuities [27,28]. Therefore, peridynamics is useful to solve problems involving spontaneously emerged discontinuities. With the general applicability of peridynamics, many applications of the method have been studied. Silling and Askari [29] wrote the first paper on the numerical simulation using the peridynamic model. In their work, the bond-based peridynamics is employed to study the convergence in a fracture problem and impact of a sphere on a brittle target. Dayal and Bhattacharya [30] studied the kinetics of phase transformations using peridynamics without any additional kinetic relation or the nucleation criterion. By adding pairwise peridynamic moments, Gerstle et al. [31] proposed a micropolar peridynamic model. Other applications of peridynamics include modeling of the structural responses under extreme loading [32], structural stability and failure analyses [33], fracture analyses [34–37], and nucleation analyses of a crack in a solid body [38]. Peridynamics also has been applied to study the effect of fiber directions in composites on the fracture and damage evolution considering anisotropic properties [39–43]. A generalized formulation of bond-based peridynamics was introduced by Silling et al. [44], which is called the state-based peridynamics. The convergence of peridynamic states to classical elasticity was studied by Silling and Lehoucq [45], and it is shown that the peridynamic stress tensor converges to the Piola–Kirchhoff stress tensor as the length scale goes to zero. Using the state-based peridynamic method, Warren et al. [46] studied the elastic deformation and fracture of a bar. Littlewood [47] presented fragmentation of an expanding tube modeled with state-based peridynamics. Foster et al. [48,49] studied viscoplasticity and the failure criterion for peridynamic states.

Compared with FEM, peridynamics is computationally expensive. Macek and Silling [50] implemented peridynamics in a commercial finite element analysis code, ABAQUS, using truss elements. The conventional FE mesh is coupled with the peridynamic truss mesh using the embedded element feature available in the finite element analysis code. Lall et al. [51] used the peridynamics based finite element model to study shock and vibration reliability of electronics. Kilic and Madenci [52] presented a coupling approach using overlapping regions in which both peridynamic and FE equations are utilized. Agwai et al. [53] and Oterkus [54] employed the submodeling approach to couple the FEM with peridynamics. In their approach, the global analysis by means of finite element analysis is performed first, and then peridynamics is used for submodeling. A morphing strategy based on the energy equivalence was proposed by Lubineau et al. [55]. In the present paper, we introduce a coupling approach of discretized peridynamics with finite elements. Different from the approach in [50,51] implementing peridynamic model in the framework of the conventional FEM and the submodeling approach [53,54], the peridynamic subregion is directly coupled to the finite element subregion in the present approach. An interface element is introduced to calculate coupling forces instead of using overlapping regions [52] or the morphing strategy [55] to couple peridynamic and FE subregions. Depending on how coupling forces are divided to FE nodes of an interface element, we further discuss two types of coupling schemes.

The remainder of this paper is organized as follows. In Section 2, the peridynamic theory and finite element formulations are summarized. In Section 3, we present two types of coupling schemes depending on the distributing schemes of coupling forces to FE

nodes of interface elements, and the inverse isoparametric mapping that is essential in the coupling approach is summarized. In Section 4, numerical examples under quasi-static conditions are provided to validate the proposed coupling approach including one- and three-dimensional elastic problems and the mixed mode fracture in a double-edge-notched concrete specimen. The results by applying two types of coupling schemes for numerical simulations are discussed. In the last section, concluding remarks are summarized.

2. Theory

2.1. Peridynamic theory

In the peridynamic theory, the equation of motion of a material point at \mathbf{x} in the reference configuration at time t , as shown in Fig. 1, is written as [27,56,57]

$$\rho \ddot{\mathbf{u}}(\mathbf{x}, t) = \int_{\mathcal{H}_{\mathbf{x}}} \mathbf{f}(\boldsymbol{\eta}, \boldsymbol{\xi}) dV_{\mathbf{x}'} + \mathbf{b}(\mathbf{x}, t), \quad (1)$$

where ρ is the mass density, \mathbf{u} is the displacement vector, \mathbf{f} is a pairwise force vector that the material point at \mathbf{x}' exerts on the material point at \mathbf{x} , $\mathcal{H}_{\mathbf{x}}$ is a neighborhood of the material point at \mathbf{x} , and \mathbf{b} is the body force density field. The relative position vector in the reference configuration, which is shown in Fig. 2(a), is expressed as [29]

$$\boldsymbol{\xi} = \mathbf{x}' - \mathbf{x}, \quad (2)$$

and the relative displacement vector at time t is written as

$$\boldsymbol{\eta} = \mathbf{u}(\mathbf{x}', t) - \mathbf{u}(\mathbf{x}, t). \quad (3)$$

For each material, a scalar δ , called the horizon, is assumed to exist to determine the interacting spatial range between the material point at \mathbf{x} and the material point at \mathbf{x}' such that

$$\mathbf{f}(\boldsymbol{\eta}, \boldsymbol{\xi}) = \mathbf{0} \quad \forall \boldsymbol{\eta} \quad \text{if } \|\boldsymbol{\xi}\| > \delta, \quad (4)$$

where $\|\cdot\|$ is the Euclidean norm. The pairwise force vector \mathbf{f} shown in Fig. 2(b) in the bond-based peridynamics is expressed as

$$\mathbf{f}(\boldsymbol{\eta}, \boldsymbol{\xi}) = f(\boldsymbol{\eta}, \boldsymbol{\xi}) \frac{\boldsymbol{\eta} + \boldsymbol{\xi}}{\|\boldsymbol{\eta} + \boldsymbol{\xi}\|}, \quad (5)$$

where f is a scalar-valued pairwise force. The bond stretch s is defined as

$$s(t, \boldsymbol{\eta}, \boldsymbol{\xi}) = \frac{\|\boldsymbol{\eta} + \boldsymbol{\xi}\| - \|\boldsymbol{\xi}\|}{\|\boldsymbol{\xi}\|}, \quad (6)$$

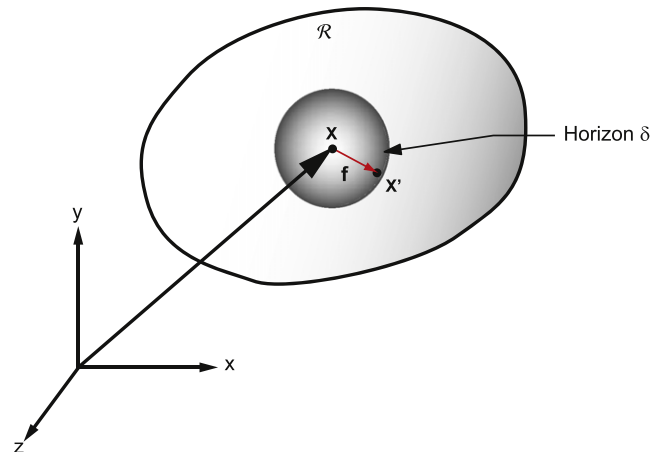


Fig. 1. Schematic of peridynamics.

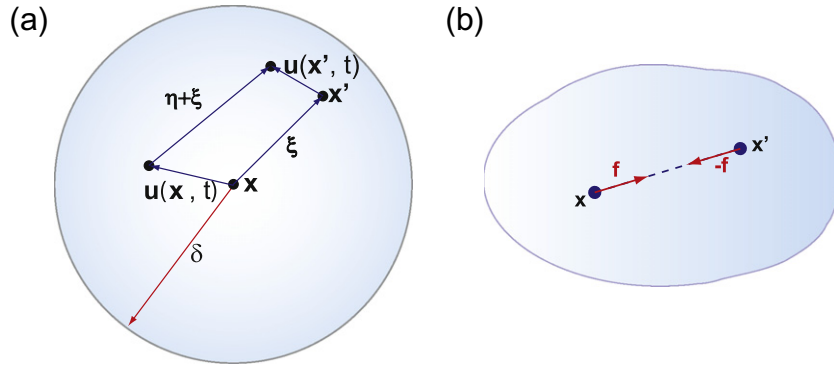


Fig. 2. (a) Relationships among the relative position vector and the relative displacement vector within a peridynamic horizon and (b) pairwise force vector.

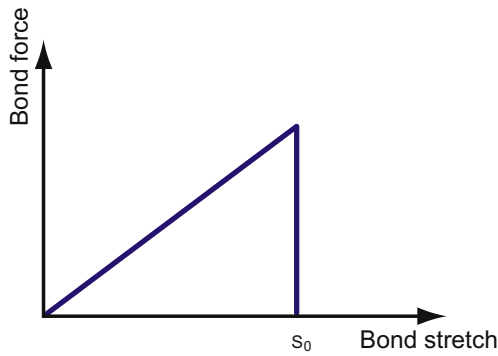


Fig. 3. Microbrittle material model.

where $\|\xi\|$ is the original bond length in the reference configuration, and $\|\eta + \xi\|$ is the deformed bond length. If the bond stretch $s = 0$, then there is no pairwise force f between material points.

Fig. 3 shows a microbrittle material model defined for peridynamic bonds. The bond force, which is a scalar function of the bond stretch s , is

$$f(\eta, \xi) = cs(t, \eta, \xi)\mu(t, \eta, \xi), \quad (7)$$

where c is the micromodulus, and μ is the scalar function to determine the bond failure. The micromodulus c can be determined by equating the strain energy density in the classical elasticity [29] or by numerical calculations [56]. The numerically determined

Table 1
Micromodulus c_1 in one-dimensional domain.

| Horizon δ | Micromodulus c_1 (N/m ⁶) |
|------------------|--|
| $2\Delta x$ | $\frac{E}{2\Delta x^4}$ |
| $3\Delta x$ | $\frac{2E}{9\Delta x^4}$ |
| $4\Delta x$ | $\frac{E}{8\Delta x^4}$ |
| $5\Delta x$ | $\frac{2E}{25\Delta x^4}$ |

Table 2
Micromodulus c_3 in three-dimensional domain.

| Horizon δ | Micromodulus c_3 (N/m ⁶) |
|------------------|--|
| $2\Delta x$ | $0.302942 \frac{E}{\Delta x^4}$ |
| $3\Delta x$ | $0.052385 \frac{E}{\Delta x^4}$ |
| $4\Delta x$ | $0.017290 \frac{E}{\Delta x^4}$ |
| $5\Delta x$ | $0.006819 \frac{E}{\Delta x^4}$ |

micromoduli, obtained by considering a finite number of bonds within the horizon, are summarized in Tables 1 and 2 for one- and three-dimensional models, respectively. The critical stretch for bond failure is denoted as s_0 . Once a bond fails, it cannot sustain force any more. The critical bond stretch s_0 for microbrittle materials is obtained by setting the work required to break all the bonds per unit fracture area identical to the energy release rate G_f [29]:

$$s_0 = \sqrt{\frac{5G_f}{9k\delta}}. \quad (8)$$

By considering broken bonds, damage dependencies can be introduced into the critical bond stretch [29,34]. The scalar function μ is related with the critical bond stretch as

$$\mu(t, \eta, \xi) = \begin{cases} 1 & \text{if } s(t', \eta, \xi) < s_0 \text{ for all } 0 \leq t' \leq t, \\ 0 & \text{otherwise.} \end{cases} \quad (9)$$

To solve the peridynamic equation of motion, the material domain is discretized with a number of nodes. The distances of two adjacent nodes are identical over the domain and denoted as Δx . Therefore, the volume representation of each node is $(\Delta x)^3$. The peridynamic equation of motion after discretization is written as

$$\rho \ddot{\mathbf{u}}_I^t = \sum_{J=1}^{N_{H_I}} \mathbf{f}(\eta^t, \xi) V_J + \mathbf{b}_I^t, \quad (10)$$

where $\ddot{\mathbf{u}}_I^t$ is the acceleration of the node I at time t , $\mathbf{f}(\eta^t, \xi)$ is the pairwise force, N_{H_I} is the total number of nodes within the horizon of the node I , and \mathbf{b}_I^t is the body force at time t . The damage index of a node is defined as [29]

$$\varphi(\mathbf{x}_I, t) = 1 - \frac{\sum_{J=1}^{N_{H_I}} \mu(t, \eta, \xi) V_J}{\sum_{J=1}^{N_{H_I}} V_J}. \quad (11)$$

In order to consider the volume reduction of a node that has an intersection with the horizon boundary, a volume reduction scheme [58] is introduced as follows:

$$V_J(\|\xi\|) = \begin{cases} \left(\frac{\delta - \|\xi\|}{2r_j} + \frac{1}{2}\right) V_J & \text{if } (\delta - r_j) \leq \|\xi\| \leq \delta \\ V_J & \text{if } \|\xi\| \leq (\delta - r_j) \\ 0 & \text{otherwise} \end{cases}, \quad (12)$$

where $(\delta - r_j)$ is the distance from which the volume is reduced, and r_j is set to be the half of the grid spacing Δx in the numerical implementation.

2.2. Finite element formulations

The equation of motion in the conventional continuum mechanics is derived from the principle of linear momentum.

The temporal change rate of linear momentum is equal to the force applied on the body as [59]

$$\rho \ddot{u}_i = \sigma_{ij,j} + f_i^B \quad \text{in } \Omega, \quad (13)$$

where ρ is the density, \ddot{u}_i is the acceleration field, σ_{ij} is the Cauchy stress tensor, and f_i^B is the body force density field. The essential boundary condition Γ_u and natural boundary condition Γ_f are defined, respectively, as [60]

$$u_i = U_i \quad \text{on } \Gamma_u, \quad (14)$$

$$\sigma_{ij} n_j = F_i^s \quad \text{on } \Gamma_f, \quad (15)$$

where the surface of the body $\Gamma = \Gamma_u \cup \Gamma_f$, $\Gamma_u \cap \Gamma_f = \emptyset$, and n_j means the components of the unit outer normal vector on Γ . The constitutive equation for continuum is stated as

$$\sigma_{ij} = C_{ijkl} \varepsilon_{kl}, \quad (16)$$

where C_{ijkl} is the elastic constitutive coefficient, and the components of strains are defined as

$$\varepsilon_{ij} = \frac{1}{2} (u_{i,j} + u_{j,i}). \quad (17)$$

Applying the principle of virtual work to Eq. (13), we have

$$\int_{\Omega} (\sigma_{ij,j} + f_i^B - \rho \ddot{u}_i) \delta u_i d\Omega = 0, \quad (18)$$

where δu_i is the virtual displacement. After integrating by parts and applying the divergence theorem, the weak formulation is obtained as [61]

$$-\int_{\Omega} \sigma_{ij} \delta u_{i,j} d\Omega + \int_{\Gamma} \sigma_{ij} n_j \delta u_i dS + \int_{\Omega} f_i^B \delta u_i d\Omega - \int_{\Omega} \rho \ddot{u}_i \delta u_i d\Omega = 0. \quad (19)$$

Considering the symmetry of the stress tensor ($\sigma_{ij} = \sigma_{ji}$) and applying the boundary conditions, we have

$$\int_{\Omega} \rho \ddot{u}_i \delta u_i d\Omega + \int_{\Omega} \sigma_{ij} \delta \varepsilon_{ij} d\Omega = \int_{\Gamma_f} F_i^s \delta u_i dS + \int_{\Omega} f_i^B \delta u_i d\Omega. \quad (20)$$

Substituting the constitutive law in Eq. (16) into Eq. (20), we obtain the finite element formulation

$$\int_{\Omega} \rho \ddot{u}_i \delta u_i d\Omega + \int_{\Omega} C_{ijkl} \varepsilon_{kl} \delta \varepsilon_{ij} d\Omega = \int_{\Gamma_f} F_i^s \delta u_i dS + \int_{\Omega} f_i^B \delta u_i d\Omega. \quad (21)$$

In the finite element analysis, the displacements within each element are interpolated by means of shape functions as [60]

$$\mathbf{u}^{(e)} = \mathbf{H}^{(e)} \mathbf{U}^{(e)}, \quad (22)$$

where $\mathbf{H}^{(e)}$ is the displacement interpolation matrix, the superscript e represents the element e , and the nodal displacement vector $\mathbf{U}^{(e)}$ is expressed as $\mathbf{U}^{(e)T} = \{u_1 v_1 w_1 \dots u_n v_n w_n\}$ for an element of n nodes. The strain vector is evaluated by

$$\boldsymbol{\varepsilon}^{(e)} = \mathbf{B}^{(e)} \mathbf{U}^{(e)}, \quad (23)$$

where $\mathbf{B}^{(e)}$ is the strain–displacement matrix which is written as

$$\mathbf{B}^{(e)} = \begin{bmatrix} \frac{\partial h_1}{\partial x} & & & & \frac{\partial h_n}{\partial x} & & \\ & \frac{\partial h_1}{\partial y} & & & & \frac{\partial h_n}{\partial y} & \\ & & \frac{\partial h_1}{\partial z} & & & & \frac{\partial h_n}{\partial z} \\ & & & \dots & & & \\ \frac{\partial h_1}{\partial y} & \frac{\partial h_1}{\partial x} & & & \frac{\partial h_n}{\partial y} & \frac{\partial h_n}{\partial x} & \\ & \frac{\partial h_1}{\partial z} & \frac{\partial h_1}{\partial y} & & \frac{\partial h_n}{\partial z} & \frac{\partial h_n}{\partial y} & \\ \frac{\partial h_1}{\partial z} & \frac{\partial h_1}{\partial x} & & & \frac{\partial h_n}{\partial z} & \frac{\partial h_n}{\partial x} & \end{bmatrix}. \quad (24)$$

Substituting Eqs. (22) and (23) into Eq. (21), we have the weak formulation in matrix form as

$$\mathbf{M} \ddot{\mathbf{U}} + \mathbf{K} \mathbf{U} = \mathbf{F}, \quad (25)$$

where \mathbf{M} is the mass matrix, \mathbf{K} is the stiffness matrix, and \mathbf{F} is the force vector. The assembled matrices following the convention of direct stiffness method [60] are summarized as

$$\mathbf{M} = \sum_e \mathbf{M}^{(e)}, \quad \mathbf{M}^{(e)} = \int_{\Omega^{(e)}} \rho^{(e)} \mathbf{H}^{(e)T} \mathbf{H}^{(e)} d\Omega^{(e)}, \quad (26)$$

$$\mathbf{K} = \sum_e \mathbf{K}^{(e)}, \quad \mathbf{K}^{(e)} = \int_{\Omega^{(e)}} \mathbf{B}^{(e)T} \mathbf{C}^{(e)} \mathbf{B}^{(e)} d\Omega^{(e)}, \quad (27)$$

$$\mathbf{F} = \sum_e \mathbf{F}_s^{(e)} + \sum_e \mathbf{F}_B^{(e)}, \quad \mathbf{F}_s^{(e)} = \int_{\Gamma_f^{(e)}} \mathbf{H}^{(e)T} \mathbf{F}^s dS^{(e)}, \quad \mathbf{F}_B^{(e)} = \int_{\Omega^{(e)}} \mathbf{H}^{(e)T} \mathbf{f}^B d\Omega^{(e)}. \quad (28)$$

3. Coupling between the peridynamic and finite element subregions

3.1. Coupling schemes

To gain the efficiency from finite element analyses and exploit the generality of peridynamics in the presence of discontinuities, a domain is partitioned into a conventional FE subregion and a peridynamic subregion as shown in Fig. 4. With the coupling approach, the subregion where failure is expected can be modeled using peridynamics. The overall computational cost is reduced by using FEM for the remainder of the domain.

In the conventional FE subregion, the lumped mass matrix is formed by distributing the total element mass to nodes of the element [60]. The internal forces on FE nodes can be calculated as

$$\mathbf{F}^{int} = \sum_e \mathbf{F}^{int(e)} = \sum_e \mathbf{K}^{(e)} \mathbf{U}^{(e)}, \quad (29)$$

where $\mathbf{K}^{(e)}$ is the element stiffness matrix. The equation of motion of an FE node is obtained as

$$M_I \ddot{\mathbf{U}}_I = \mathbf{F}_I^{ext} - \mathbf{F}_I^{int}, \quad (30)$$

where M_I is the lumped mass of node I , $\ddot{\mathbf{U}}_I$ is the acceleration vector field, \mathbf{F}_I^{ext} is the external force applied on the node I by evaluating the corresponding components of \mathbf{F} in Eq. (28), and \mathbf{F}_I^{int} is the internal force vector of the node I . Because the mass matrix is diagonal, Eq. (30) can be solved without factorizing a global stiffness matrix.

To bridge the FE subregion and the peridynamic subregion, we introduce an interface element. A three-dimensional interface element consisting of eight FE nodes is illustrated in Fig. 5. In an interface element, a number of peridynamic nodes are embedded for the calculation of coupling forces. The interacting forces between embedded peridynamic nodes and peridynamic nodes out of interface elements are called coupling forces. It is worth noting that interactions between embedded peridynamic nodes are not considered as coupling forces. The number of embedded peridynamic nodes is determined by the size of the horizon, and there should be sufficient embedded nodes within the horizon of nodes near the interface of the peridynamic subregion and the FE subregion as shown in Fig. 5. To evaluate coupling forces, each embedded peridynamic node represents a material volume of $(\Delta x)^3$ inside an interface element. However, embedded peridynamic nodes are not involved in the global equation. In other words, the displacements of embedded peridynamic nodes are not calculated by solving the equation of motion. Therefore, the mass of an interface element is equally distributed to FE nodes of the interface element. Consider an embedded peridynamic node subjected to the coupling force \mathbf{F}^{cp} as shown in Fig. 6, the coupling force is then divided to FE nodes of the interface element by means of shape functions as

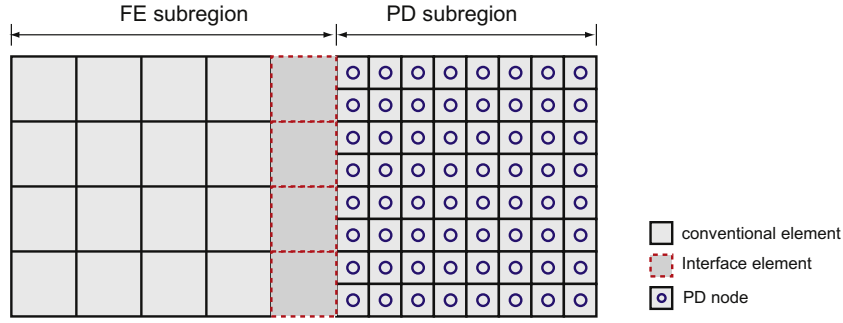


Fig. 4. Partitions of the domain. The FE subregion and the peridynamic (PD) subregion are bridged by interface elements.

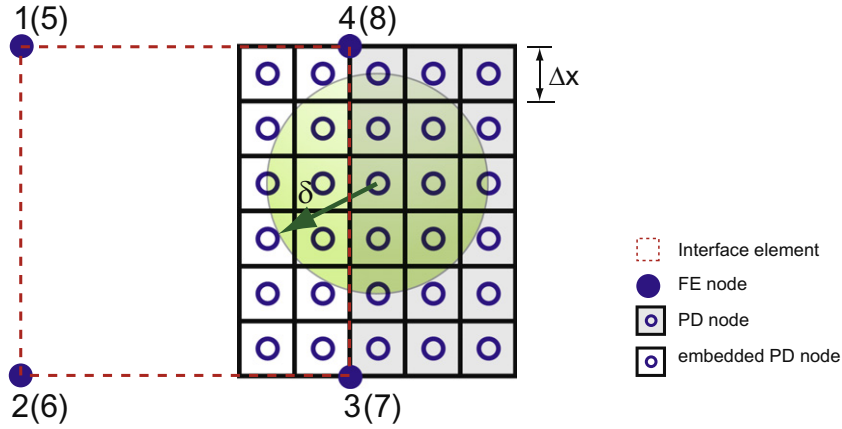


Fig. 5. Interface element for the coupling of FE subregion and peridynamic subregion.

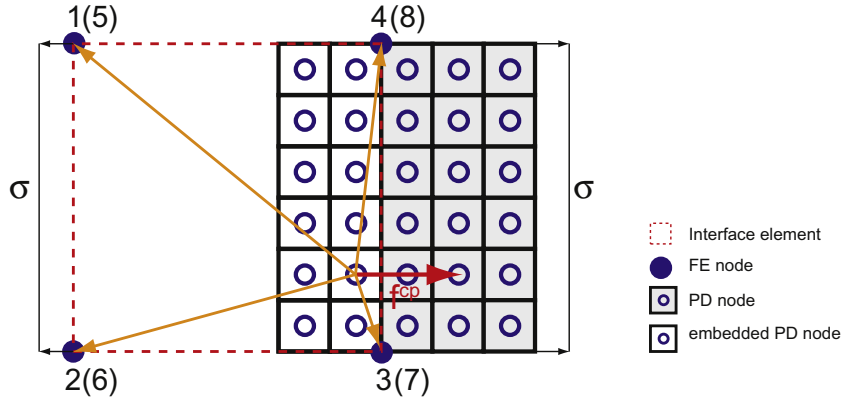


Fig. 6. VL-coupling scheme that divides a coupling force \mathbf{f}^{cp} to FE nodes of the interface element.

$$\mathbf{f}_i^{cp} = \phi_i(\xi, \eta, \psi) \mathbf{f}^{cp}, \quad i = 1, \dots, 8, \quad (31)$$

where ϕ_i is the shape function of the node i belonging to the interface element, (ξ, η, ψ) are the natural coordinates of the embedded node in the interface element, which should be determined by the inverse isoparametric mapping. We designate this coupling scheme as the *VL-coupling scheme* since the whole volume of the interface element is subjected to coupling forces. On the other hand, different from the VL-coupling scheme, we might divide coupling forces only to the FE nodes on the interface segment as shown in Fig. 7. Therefore, FE nodes not on the interface segment are subjected to internal forces arising from the element stiffness only. Since the interface between the peridynamic and FE subregions is similar to a contact surface, the scheme demonstrated in Fig. 7 is designated as the

CT-coupling scheme. To implement the CT-coupling scheme, interfaces between the peridynamic subregion and the FE subregion have to be defined prior to analyses. Coupling forces on embedded nodes are divided to those FE nodes on the interface segment as shown in Fig. 7 by

$$\mathbf{f}_i^{cp} = \phi_i(\xi_c, \eta_c) \mathbf{f}^{cp}, \quad i = 3, 4, 7, 8, \quad (32)$$

where ϕ_i is the shape function on the interface segment, and (ξ_c, η_c) are the natural coordinates of the projection of an embedded node onto the interface segment.

In general, the equation of motion for FE nodes of an interface element is written as

$$M_I \ddot{\mathbf{U}}_I = \mathbf{F}_I^{ext} - \hat{\mathbf{F}}_I^{int}, \quad (33)$$

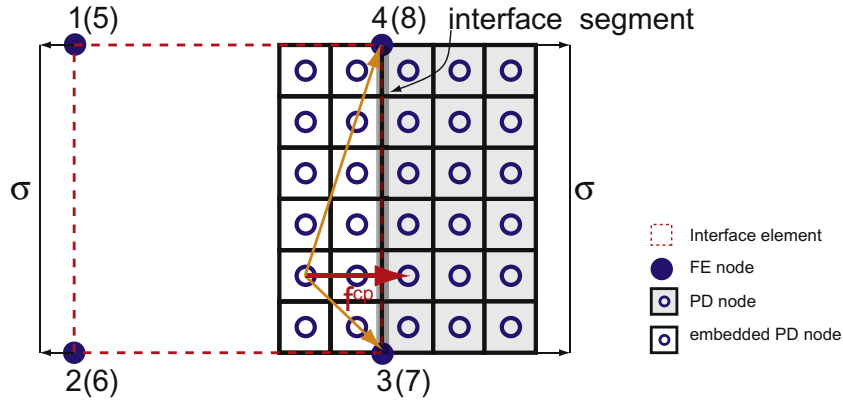


Fig. 7. CT-coupling scheme that divides a coupling force \mathbf{f}^{cp} to FE nodes on the interface segment.

where \mathbf{F}_I^{ext} is the external force by evaluating Eq. (28), and the internal force is given as

$$\hat{\mathbf{F}}_I^{int} = \mathbf{F}_I^{int} + \mathbf{f}_I^{cp} = \left[\sum_e \mathbf{K}^{(e)} \mathbf{U}^{(e)} \right]_I + \mathbf{f}_I^{cp}, \quad (34)$$

in which $[\cdot]_I$ denotes the corresponding components of a vector associated with the node I of the interface element, and \mathbf{f}_I^{cp} is the summation of coupling forces on the node I . The explicit algorithm is employed for the transient dynamic analyses. Nodal accelerations are calculated first, nodal velocities and displacements are updated subsequently. After the displacements of FE nodes of the interface elements are calculated, the displacements of embedded peridynamic nodes are then determined by

$$\mathbf{U}_{eb} = \phi_i(\xi, \eta, \psi) \mathbf{U}_i, \quad i = 1, \dots, 8, \quad (35)$$

in which (ξ, η, ψ) are the natural coordinates of an embedded peridynamic node in the interface element, and \mathbf{U}_i is the nodal displacement of an interface element. For peridynamic nodes out of the interface elements, Eq. (10) is used to update nodal accelerations.

3.2. Inverse isoparametric mapping

To couple peridynamic subregions with finite element subregions, a certain number of peridynamic nodes are embedded in the interface elements. If the Cartesian coordinates of an embedded peridynamic node are known, the natural coordinates of the embedded peridynamic node in an interface element should be determined by the inverse isoparametric mapping, which is essential especially for random discretizations. However, the inverse isoparametric mapping from the Cartesian coordinates to the natural coordinates is nontrivial since equations to be solved are nonlinear. Murti and Valliappan [62] presented a numerical technique by bisecting a line passing a point and a node of known natural coordinates, and this method was extended to the three-dimensional space by Murti et al. [63]. However, the bisection method has its limitations [64]. A more generalized approach for the inverse isoparametric mapping is presented by Chinnaswamy et al. [64]. For the inverse mapping of an embedded peridynamic node with known Cartesian coordinates $(\hat{x}, \hat{y}, \hat{z})$, the equation to be solved is written as

$$\mathbf{f} = \begin{Bmatrix} f_1(\xi, \eta, \psi) \\ f_2(\xi, \eta, \psi) \\ f_3(\xi, \eta, \psi) \end{Bmatrix} = \begin{Bmatrix} \sum_{i=1}^n \phi_i(\xi, \eta, \psi) x_i - \hat{x} \\ \sum_{i=1}^n \phi_i(\xi, \eta, \psi) y_i - \hat{y} \\ \sum_{i=1}^n \phi_i(\xi, \eta, \psi) z_i - \hat{z} \end{Bmatrix} = \begin{Bmatrix} 0 \\ 0 \\ 0 \end{Bmatrix}, \quad (36)$$

where (ξ, η, ψ) are the natural coordinates of an embedded peridynamic node in an interface element to be determined. By expanding

the vector \mathbf{f} in Taylor's series and omitting the second and higher order terms, it can be shown that [64]

$$\mathbf{I} = \mathbf{I}_0 - \begin{bmatrix} \frac{\partial f_1}{\partial \xi} & \frac{\partial f_1}{\partial \eta} & \frac{\partial f_1}{\partial \psi} \\ \frac{\partial f_2}{\partial \xi} & \frac{\partial f_2}{\partial \eta} & \frac{\partial f_2}{\partial \psi} \\ \frac{\partial f_3}{\partial \xi} & \frac{\partial f_3}{\partial \eta} & \frac{\partial f_3}{\partial \psi} \end{bmatrix}_0^{-1} \mathbf{f}_0, \quad (37)$$

where $\mathbf{I}_0 = [\xi_0, \eta_0, \psi_0]^T$ is an approximate solution, and \mathbf{f}_0 is the vector \mathbf{f} evaluated at the approximate solution \mathbf{I}_0 . Eq. (37) can be rewritten as

$$\mathbf{I} = \mathbf{I}_0 - \begin{bmatrix} \sum \frac{\partial \phi_i}{\partial \xi} x_i & \sum \frac{\partial \phi_i}{\partial \eta} x_i & \sum \frac{\partial \phi_i}{\partial \psi} x_i \\ \sum \frac{\partial \phi_i}{\partial \xi} y_i & \sum \frac{\partial \phi_i}{\partial \eta} y_i & \sum \frac{\partial \phi_i}{\partial \psi} y_i \\ \sum \frac{\partial \phi_i}{\partial \xi} z_i & \sum \frac{\partial \phi_i}{\partial \eta} z_i & \sum \frac{\partial \phi_i}{\partial \psi} z_i \end{bmatrix}_0^{-1} \begin{Bmatrix} \sum \phi_i x_i - \hat{x} \\ \sum \phi_i y_i - \hat{y} \\ \sum \phi_i z_i - \hat{z} \end{Bmatrix}, \quad (38)$$

and it can be simplified as

$$\mathbf{I} = \mathbf{I}_0 + \Delta \mathbf{I}, \quad (39)$$

where

$$\Delta \mathbf{I} = \begin{Bmatrix} \Delta \xi \\ \Delta \eta \\ \Delta \psi \end{Bmatrix} = -\mathbf{J}_0^{-1} \mathbf{f}_0. \quad (40)$$

The updated solution of \mathbf{I} is used as the value of \mathbf{I}_0 in Eq. (39) for the next iteration. A few iterations are performed till the solution of \mathbf{I} converges.

If the CT-coupling scheme is employed, coupling forces on embedded peridynamic nodes are only distributed to FE nodes on the interface segment as shown in Fig. 7. Hence, the natural coordinates of the projection of an embedded peridynamic node

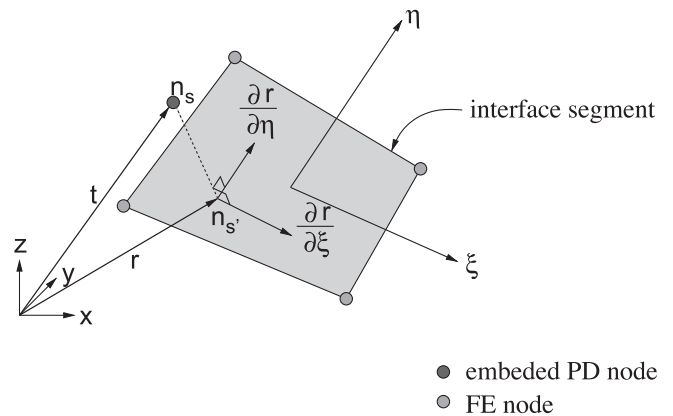


Fig. 8. Projection of an embedded peridynamic node on an interface segment.

onto the interface segment have to be determined. Let \mathbf{t} be the position vector of an embedded node n_s , and the projection of n_s onto the interface segment is denoted by $n_{s'}$ as shown in Fig. 8. The position vector \mathbf{r} of the point $n_{s'}$ on the interface segment can be expressed as

$$\mathbf{r} = f_1(\xi_c, \eta_c)\mathbf{e}_1 + f_2(\xi_c, \eta_c)\mathbf{e}_2 + f_3(\xi_c, \eta_c)\mathbf{e}_3, \quad (41)$$

where (ξ_c, η_c) are the natural coordinates of the point $n_{s'}$ on the interface segment, and

$$f_i(\xi, \eta) = \sum_{j=1}^4 \phi_j x_i^j, \quad (42)$$

in which ϕ_j is the shape function of the node j on the interface segment. The natural coordinates (ξ_c, η_c) of the point $n_{s'}$ on the interface segment must satisfy [65]

$$\frac{\partial \mathbf{r}}{\partial \xi} \cdot (\mathbf{t} - \mathbf{r}) = 0, \quad (43)$$

$$\frac{\partial \mathbf{r}}{\partial \eta} \cdot (\mathbf{t} - \mathbf{r}) = 0. \quad (44)$$

However, there is no analytical solution to Eqs. (43) and (44). To solve numerically, a few iterations of the least-squares projection are used to generate an initial guess as

$$\xi_0 = 0, \quad \eta_0 = 0, \quad (45)$$

$$\begin{bmatrix} \mathbf{r}_{,\xi} \cdot \mathbf{r}_{,\xi} & \mathbf{r}_{,\xi} \cdot \mathbf{r}_{,\eta} \\ \mathbf{r}_{,\eta} \cdot \mathbf{r}_{,\xi} & \mathbf{r}_{,\eta} \cdot \mathbf{r}_{,\eta} \end{bmatrix} \begin{Bmatrix} \Delta \xi \\ \Delta \eta \end{Bmatrix} = - \begin{Bmatrix} \mathbf{r}_{,\xi} \cdot (\mathbf{r} - \mathbf{t}) \\ \mathbf{r}_{,\eta} \cdot (\mathbf{r} - \mathbf{t}) \end{Bmatrix}, \quad (46)$$

$$\xi_{i+1} = \xi_i + \Delta \xi, \quad \eta_{i+1} = \eta_i + \Delta \eta. \quad (47)$$

With an initial guess, Newton–Raphson method is then utilized to find the solution of Eqs. (43) and (44) as [66]

$$\mathbf{H} \begin{Bmatrix} \Delta \xi \\ \Delta \eta \end{Bmatrix} = - \begin{Bmatrix} \mathbf{r}_{,\xi} \cdot (\mathbf{r} - \mathbf{t}) \\ \mathbf{r}_{,\eta} \cdot (\mathbf{r} - \mathbf{t}) \end{Bmatrix}, \quad (48)$$

$$\mathbf{H} = \begin{bmatrix} \mathbf{r}_{,\xi} \cdot \mathbf{r}_{,\xi} & \mathbf{r}_{,\xi} \cdot \mathbf{r}_{,\eta} \\ \mathbf{r}_{,\eta} \cdot \mathbf{r}_{,\xi} & \mathbf{r}_{,\eta} \cdot \mathbf{r}_{,\eta} \end{bmatrix} + \begin{bmatrix} (\mathbf{r} - \mathbf{t}) \cdot \mathbf{r}_{,\xi\xi} & (\mathbf{r} - \mathbf{t}) \cdot \mathbf{r}_{,\xi\eta} \\ (\mathbf{r} - \mathbf{t}) \cdot \mathbf{r}_{,\eta\xi} & (\mathbf{r} - \mathbf{t}) \cdot \mathbf{r}_{,\eta\eta} \end{bmatrix}, \quad (49)$$

$$\xi_{i+1} = \xi_i + \Delta \xi, \quad \eta_{i+1} = \eta_i + \Delta \eta. \quad (50)$$

The solutions of ξ_{i+1} and η_{i+1} are used to update the value of the position vector \mathbf{r} , and then Eq. (48) is evaluated again for the next iteration. The converged solutions of ξ_{i+1} and η_{i+1} are the natural coordinates of the point $n_{s'}$ on the interface segment.

4. Numerical applications

4.1. One-dimensional bar

For benchmarking, the present coupling approach of peridynamics with FEM is employed to study the axial deformation of a

one-dimensional bar. The length of the bar is 9.5 mm, and dimensions of the cross section are 0.5 mm by 0.5 mm. Young's modulus E of the bar is 70 GPa, and the density is 2700 kg/m³. Fig. 9 shows the multiscale discretization of the bar. The finite element mesh size is 1.5 mm, and the conventional bar elements are utilized. The stiffness of a bar is $k = \frac{EA}{L}$, where A is the cross-sectional area and L is the length of the bar. The peridynamic grid spacing is 0.5 mm, which is equal to the width of the bar. By setting the horizon to $2\Delta x$, the one-dimensional micromodulus c_1 is 5.6×10^{23} N/m⁶. Two interface elements are used to couple peridynamic and FE subregions, and each interface element has two embedded peridynamic nodes for the calculation of coupling forces as shown in Fig. 9.

A tensile loading with the magnitude of $F = 175$ N is applied on both ends of the bar under the quasi-static condition. The force is gradually increased during 50,000 steps with the calculation time step $dt = 5 \times 10^{-8}$ s, which is less than the critical time step for the explicit time integration. Fig. 10(a) shows the displacement along the bar using the VL-coupling scheme. Nodal displacements in the peridynamic subregion show good agreement with the quasi-static solution. The displacements of the FE nodes, however, show small discrepancies. The reason is that coupling forces in an interface element are divided to all FE nodes of the element using the VL-coupling scheme so that FE nodes at the interfaces of subregions ($x = \pm 1.75$ mm) only receive partial coupling forces. FE nodes at the other end of the interface elements ($x = \pm 3.25$ mm) receive the rest of coupling forces, and are also subjected to internal forces arising from the element stiffness. Consequently, the displacements of FE nodes at the interfaces are slightly overestimated, and displacements of other FE nodes are underestimated as indicated in Fig. 10(a). In contrast, the solution using the CT-coupling scheme, which distributes coupling forces only to FE nodes at interfaces, is almost identical to the quasi-static solution as shown in Fig. 10(b). Hence, for the calculation of axial displacement, the CT-coupling scheme is more effective than the VL-coupling scheme to achieve the coupling between the peridynamic subregion and the FE subregion.

4.2. Three-dimensional bar

A three-dimensional bar subjected to tension is examined to compare the solutions of the present coupling approach and the classical (local) elasticity solutions. The dimensions of the bar are taken to be 10 mm in length, 7 mm in width, and 7 mm in thickness as shown in Fig. 11. The three-dimensional model is partitioned into two FE subregions and one peridynamic subregion. Each FE subregion consists of four eight-node solid interface elements, and the mesh size of the interface element is 3.5 mm. The peridynamic subregion is uniformly discretized with the grid spacing $\Delta x = 0.5$ mm, and the size of the horizon is set to $\delta = 1.0$ mm. In the interface element, two additional layers of peridynamic

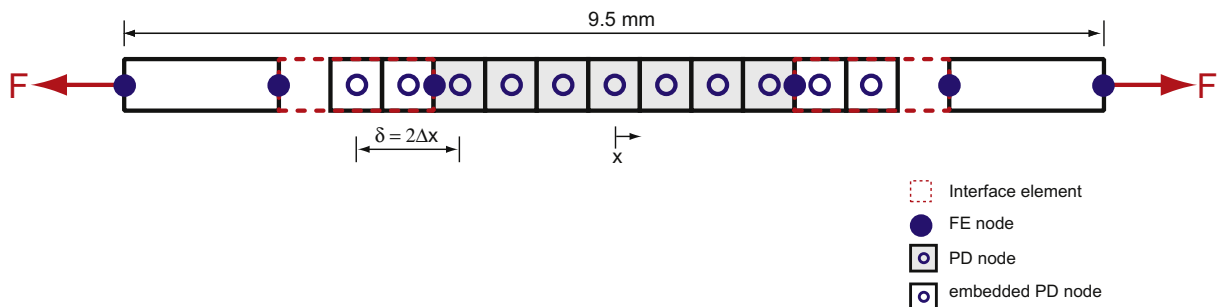


Fig. 9. Discretization of a one-dimensional bar for coupling.

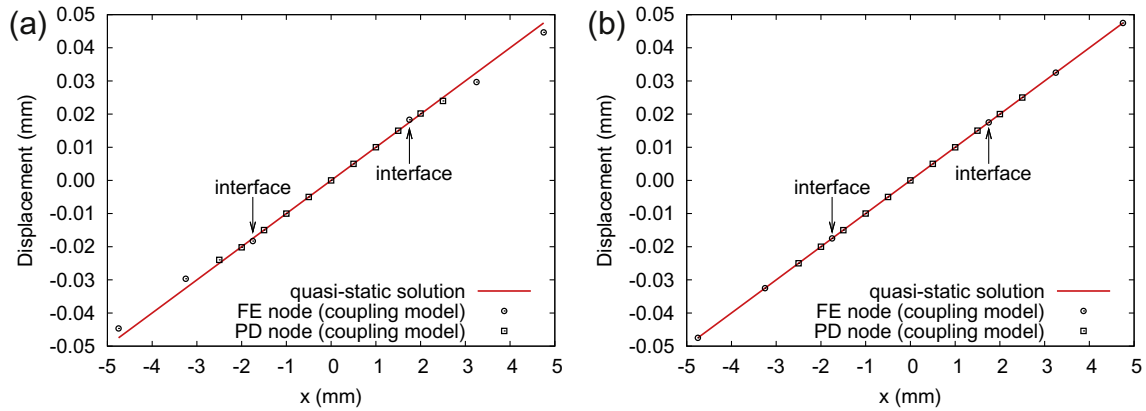


Fig. 10. Axial displacement along the bar using (a) VL-coupling scheme and (b) CT-coupling scheme.

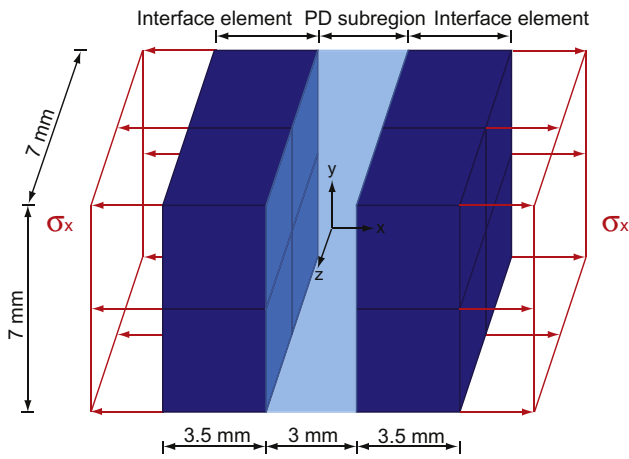


Fig. 11. Three-dimensional bar subjected to tension.

nodes are embedded along the longitudinal direction to ensure sufficient nodes in the horizon of peridynamic nodes near the interfaces. Traction at both end surfaces are gradually applied up to $\sigma_x = 700$ MPa during 100,000 steps as quasi-static loading, and the calculation time step is set to $dt = 5 \times 10^{-8}$ s. Young's modulus of the bar is 70 GPa, Poisson's ratio is 0.25, and the density is 2700 kg/m³.

We first examine the numerical solutions using the VL-coupling scheme. The longitudinal displacements u_x at three measuring

positions are compared to the quasi-static results as shown in Fig. 12(a). The displacement u_x at the position p_1 , which is at the end surface, is underestimated compared to the quasi-static solution. On the other hand, the displacement at p_2 , which is at the interface of the peridynamic subregion and the FE subregion, and the displacement at p_3 , which is inside the peridynamic subregion, show good agreement with the quasi-static solutions. To look into Poisson effect, the transverse displacements measured at different positions are plotted in Fig. 12(b). The transverse displacement q_1 at the end surface is smaller than the quasi-static value since the longitudinal displacement at the end surface is underestimated. Nevertheless, the transverse displacement q_2 at the interface demonstrates close agreement with the quasi-static solution, which indicates that Poisson effect is preserved at the interface. The transverse displacement at q_3 , which is inside the peridynamic subregion, also matches the quasi-static solution.

For the comparison of two types of coupling schemes, the CT-coupling scheme, which achieves coupling by considering the interfaces of subregions similar to contact surfaces, is then employed to study this quasi-static problem. As shown in Fig. 13(a), the longitudinal displacement p_1 at the end surface is close to the quasi-static solution with the error less than 2%. The longitudinal displacements at interface and inside the peridynamic subregion, denoted by p_2 and p_3 respectively in Fig. 13(a), are almost identical to the quasi-static solutions. The transverse displacements measured at different positions are plotted in Fig. 13(b). With the improved result in the longitudinal displacement at the end surface, the transverse displacement q_1 at the end surface turns to be very close to the quasi-static solution. On the other

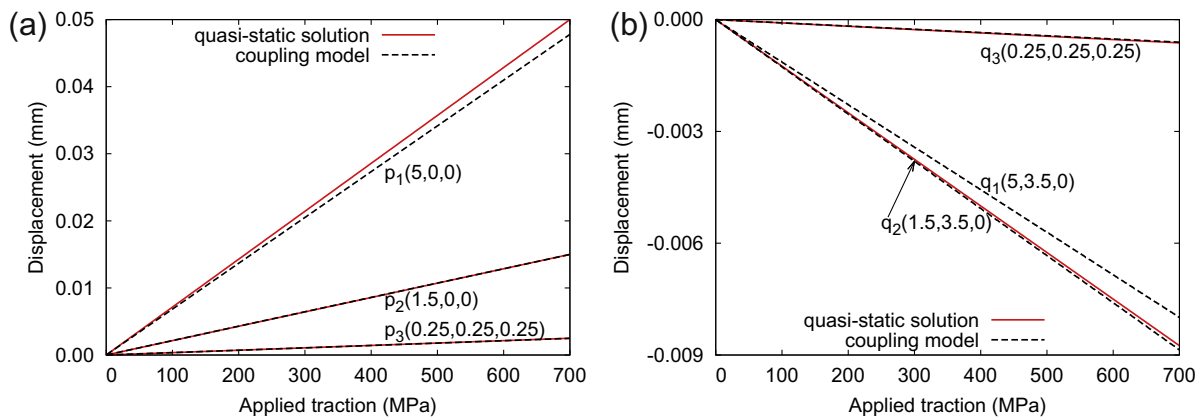


Fig. 12. Displacements (a) u_x and (b) u_y at different positions using the VL-coupling scheme. Coordinates of the measuring position are given in parenthesis.

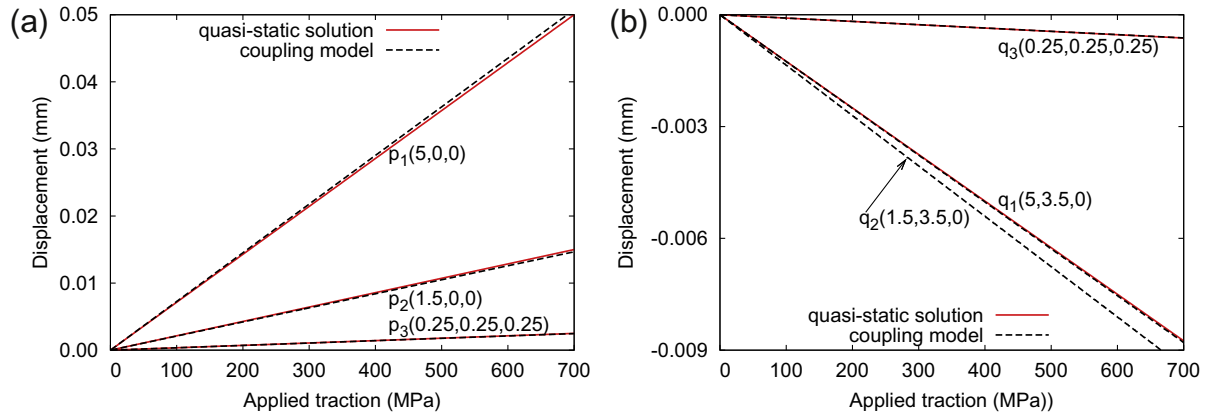


Fig. 13. Displacements (a) u_x and (b) u_y at different positions using the CT-coupling scheme. Coordinates of the measuring position are given in parenthesis.

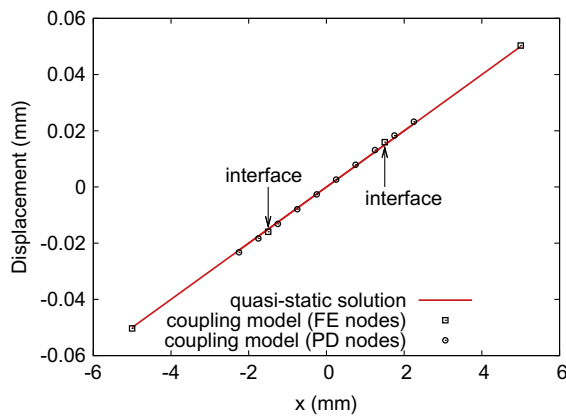


Fig. 14. Axial displacement along the edge of the bar using the CT-coupling scheme.

hand, the transverse displacement q_2 at the interface is overestimated. This phenomenon occurs due to the reason that decompositions of coupling forces in the transverse direction are divided only to FE nodes on the interface. By comparing Figs. 12 and 13, it is observed that the CT-coupling scheme is effective in resolving displacements normal to the interface of peridynamic and FE subregions. On the other hand, the VL-coupling scheme, which divides coupling forces to all FE nodes of the interface element, is capable to preserve Poisson effect at the interface.

Fig. 14 shows the longitudinal displacement along the edge of the bar solved by the CT-coupling scheme. It is noted that a smooth curve can be obtained if the nodal displacements are connected, which is different from the result in [52] where a jump in

displacement is observed at the interface. The strain ε_x distributions in the bar and at the interface are plotted in Fig. 15. Nodal strains in the FE subregions are obtained by evaluating Eq. (23), and nodal strains in the peridynamic subregion are calculated as the average bond stretch within the grid width Δx . Considering the quasi-static condition, the analytical value of strain ε_x is 0.01. The strain of the coupling model is in the range of 0.0099–0.0105 as shown in Fig. 15, which agrees with the quasi-static solution.

The essence of coupling forces is interactions between nodes in the peridynamic subregion and material volumes of an adjacent continuous body (i.e., interface elements) represented by embedded peridynamic nodes. Therefore, the ratio of the grid spacing of peridynamic nodes to the mesh size of interface elements should not affect the results. To illustrate this point, Fig. 16 shows the summation of coupling forces in the longitudinal direction on the interface elements at the left end of the bar as the applied traction increases. As indicated by the comparison in Fig. 16, differences in the results using the grid spacing $\Delta x = 1.0$ mm and $\Delta x = 0.5$ mm are insignificant.

4.3. Mixed mode fracture in a tension-shear specimen

A benchmark problem of mixed mode crack propagation in a concrete specimen has been investigated experimentally by Nooru-Mohamed et al. [19]. The double-edge-notched specimen is illustrated in Fig. 17(a). The dimensions of the specimen are taken to be 200 mm in both length and height, 50 mm in width, and two notches at edges are 25 mm in length, 5 mm in height, and 50 mm in width. For the numerical study, the specimen is partitioned into two FE subregions and one peridynamic subregion as shown in Fig. 17(b). The FE subregion is discretized with two mesh sizes, 10 mm \times 10 mm \times 16.25 mm and 10 mm \times 10 mm \times 13 mm. The

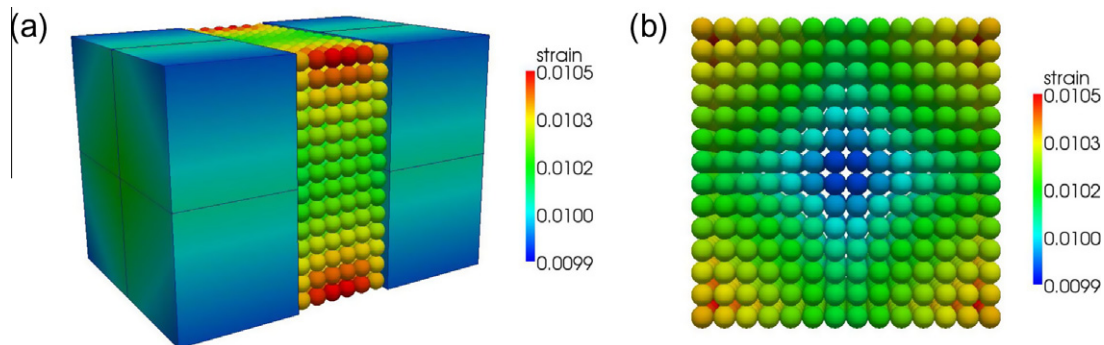


Fig. 15. Strain ε_x distributions (a) in the bar and (b) at the interface when the applied traction $\sigma_x = 700$ MPa. The CT-coupling scheme is used in the simulation.

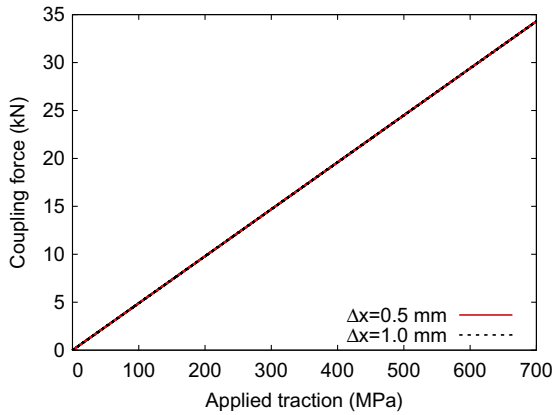


Fig. 16. Summation of coupling forces in the longitudinal direction on the interface elements at the left end of the bar. The CT-coupling scheme is used in the simulation.

peridynamic subregion is discretized with the grid spacing $\Delta x = 5.0$ mm, which is 1/10 of the specimen thickness, and the horizon is set to $\delta = 1.0$ mm. The notches in the peridynamic subregion are introduced by deleting nodes along two notches and removing all bonds across the notches. Since the ratio of the horizon to the grid spacing is equal to two, two layers of peridynamic nodes adjacent to interfaces are embedded in interface elements for the calculation of coupling forces. Young's modulus, Poisson's ratio, and fracture energy were not measured in the experiments. Therefore, we adopt the material properties $E = 30$ GPa and $G_f = 110$ J/m² as in [10]. For Poisson's ratio, it is estimated as $\nu = 0.2$ in the numerical studies in [12,10], and $\nu = 0.3$ is used in [67]. In the present study, Poisson's ratio $\nu = 0.25$ is assumed. The density is calculated from the concrete composition given in [19] as $\rho = 2265$ kg/m³. By applying Eq. (8), the critical bond stretch is obtained as $s_0 = 5.5277 \times 10^{-4}$. The brittle material model illustrated in Fig. 3 is utilized for the peridynamic subregion, and the linear elastic model is employed for the remaining FE subregions, where material parameters $E = 30$ GPa and $\nu = 0.25$ are used.

For the comparison, the load-path 1b (specimen 46–05) in [19] is considered. A horizontal shear force of 10 kN is applied first, and then the vertical displacement u_n is applied on the top and bottom of the specimen as shown in Fig. 17(a). In the numerical calculation, the time step is set to $dt = 1 \times 10^{-7}$ s, which is less than the critical

time step for the explicit time integration. The vertical displacement u_n is applied by imposing a constant velocity of 10 mm/s as quasi-static loading. We first examine the numerical predictions of crack paths using the VL-coupling scheme. The cracks initiate near the notches as shown in Fig. 18(a), and propagate along the horizontal direction for about 50 mm. As the boundary displacement increases, the direction of propagation changes as shown in Figs. 18(b) and 18(c). At the boundary displacement $u_n = 0.09$ mm, two cracks are connected as shown in Fig. 18(d). The numerical prediction of crack paths using the VL-coupling scheme shows differences with the experimental observations in [19].

We then apply the CT-coupling scheme for the numerical simulation. Interfaces are predefined in the reference configuration, and there are 280 interface segments with the given mesh sizes. Natural coordinates of the projections of embedded nodes onto interface segments are saved to a list. In the subsequent calculations, the natural coordinates of projected points are referred, and the coupling forces on embedded peridynamic nodes are divided to FE nodes on interface segments. The damage evolution is shown in Fig. 19. Crack initiation occurs at the left and right notches as shown in Fig. 19(a), and materials ahead of crack tips are damaged for the length of around 15 mm to 20 mm. Due to the angle change of the principal stress, cracks propagate with an angle as shown in Fig. 19(b). As the boundary displacement increases, two curvilinear crack paths are clearly observed in Fig. 19(c). An enclosed area is gradually formed between two curvilinear cracks as indicated in Fig. 19(d). The numerical prediction of crack paths shows agreement, especially for the lower crack, with the experimental observation presented in [19], which is illustrated using the solid line in Fig. 19(d). The small discrepancies appeared in Fig. 19(d) might be caused by the perfectly brittle material model adopted in the numerical simulation. More investigation of material models for concrete in the framework of peridynamics is required in the future. Note that the numerically predicted crack paths are in perfect symmetry. On the contrary, the cracks in the experiment do not show perfect symmetry, and we might speculate on symmetry breaking caused by the slight differences in the loading condition and the material heterogeneity.

Compared to the numerical results using the VL-coupling scheme, the results using the CT-coupling scheme demonstrate better agreement with the experimental observation. The reason for the inferiority of the VL-coupling scheme in this mixed mode fracture problem is that the horizontal displacement at edges caused by the constant shear loading is underestimated after the

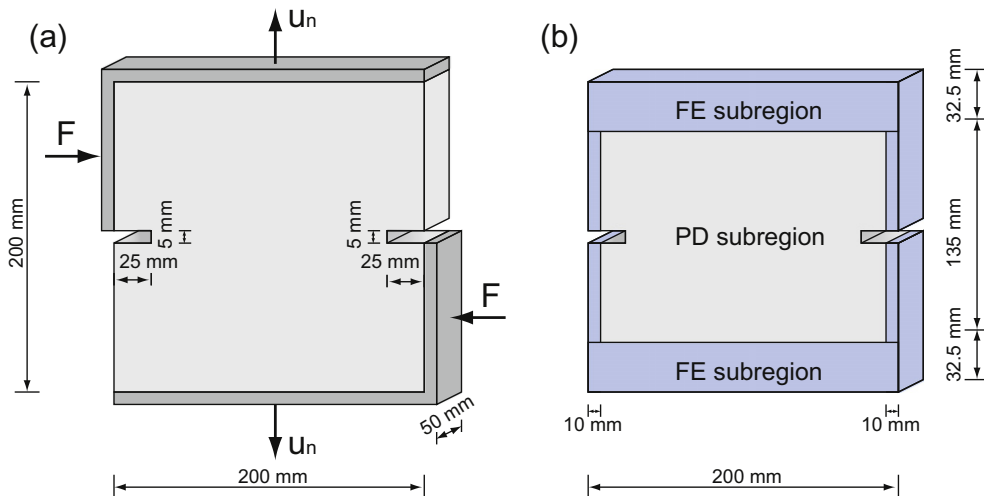


Fig. 17. Mixed mode fracture test: (a) geometry of the specimen and (b) subregions of the coupling model.

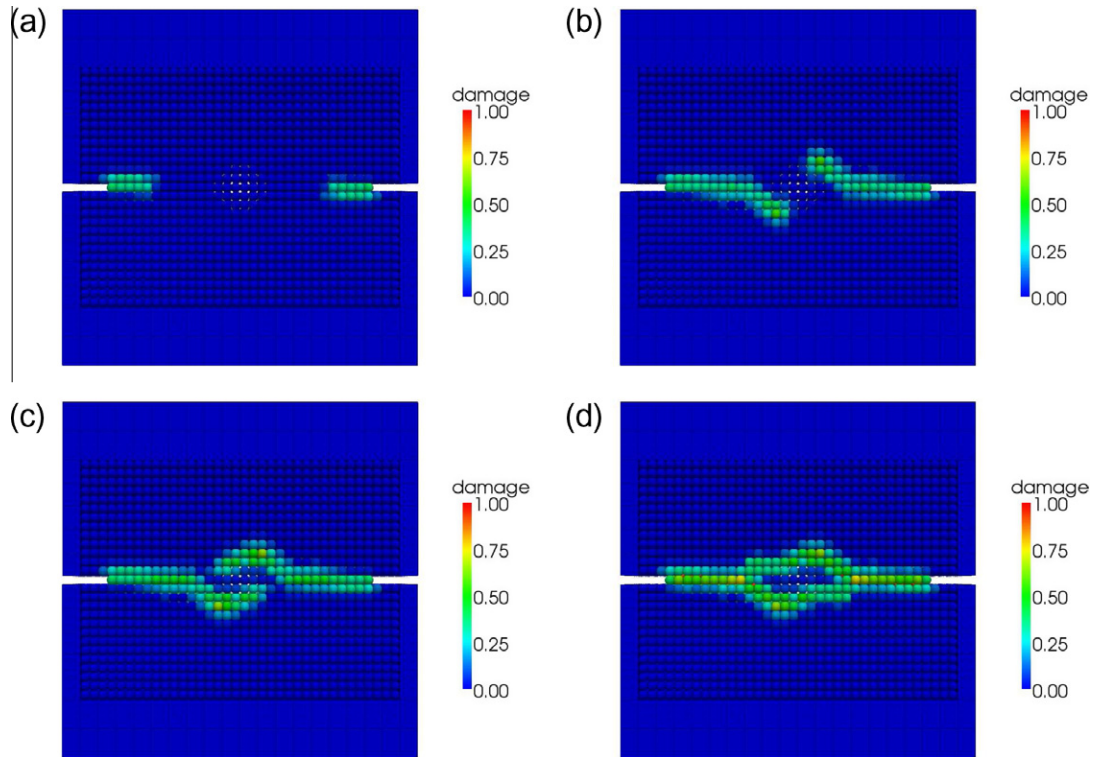


Fig. 18. Numerical prediction of crack paths using the VL-coupling scheme. Boundary displacement: (a) $u_n = 0.0220$ mm, (b) $u_n = 0.0225$ mm, (c) $u_n = 0.03$ mm and (d) $u_n = 0.09$ mm.

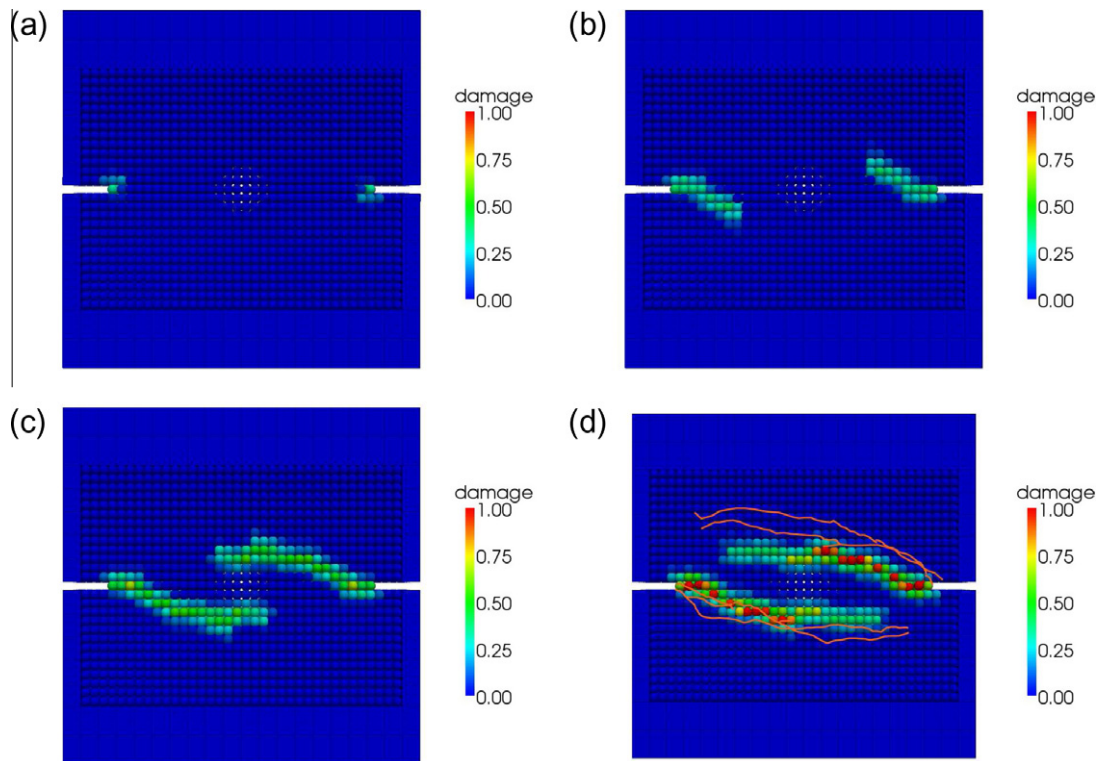


Fig. 19. Numerical prediction of crack paths using the CT-coupling scheme. Boundary displacement: (a) $u_n = 0.0220$ mm, (b) $u_n = 0.0225$ mm, (c) $u_n = 0.03$ mm and (d) $u_n = 0.09$ mm. Solid curves are crack paths observed in the experiment from [19].

applied vertical displacement at boundaries reaches the critical value for the crack initiation at two notches. Consequently, the opening-mode fracture dominates, and the large area ahead of crack

tips is damaged in the plane of notches. After the intact region in the middle of the specimen becomes relatively small, rotations of crack paths then take place as shown in Fig. 18.

5. Conclusions

A coupling approach of discretized peridynamics with FEM is presented in this paper. To bridge conventional FE subregions and peridynamic subregions, an interface element is introduced. The proposed coupling approach is different from other methods in the sense of direct coupling via interface elements. Depending on the size of the horizon, a number of peridynamic nodes are embedded in an interface element. The embedded peridynamic nodes are not involved in the global equation, but essential in the calculation of coupling forces. The coupling forces describe interactions between embedded peridynamic nodes in interface elements and peridynamic nodes in peridynamic subregions. Two types of coupling schemes are introduced. In the VL-coupling scheme, coupling forces on embedded peridynamic nodes are divided to FE nodes of interface elements. On the other hand, coupling forces are divided only to FE nodes on interface segments in the CT-coupling scheme. The inverse isoparametric mapping techniques to determined the natural coordinates of embedded peridynamic nodes in the interface elements and the natural coordinates of projected points on the interface segments are summarized.

Numerical simulations are conducted to compare the computational results using the coupling approach to the classical elasticity solutions. The axial deformation of a one-dimensional bar under quasi-static loading is studied. It is found that the displacements at interfaces of subregions are slightly overestimated, and the displacements in the FE subregions are underestimated using the VL-coupling scheme. On the other hand, the numerical solution using the CT-coupling scheme is almost identical to the quasi-static solution in all subregions and interfaces. For three-dimensional simulations, a bar subjected to quasi-static tension is partitioned into a peridynamic subregion and two FE subregions consisting of eight-node interface elements at both ends of the bar. By measuring displacements at different positions, the CT-coupling scheme is found to be effective in resolving displacements normal to the interface of peridynamic and FE subregions, and the VL-coupling scheme is capable to preserve Poisson effect at the interfaces. Longitudinal strain distributions in the bar and at the interface using the CT-coupling scheme demonstrate good agreement with the quasi-static solution.

The last numerical example is the mixed mode fracture in a concrete specimen subjected to quasi-static loading. The region where failure is expected is modeled using peridynamics, and the remaining region is modeled using conventional FEM to reduce the computational cost. Numerical predictions of crack paths using the VL-coupling scheme and the CT-coupling scheme are studied. Two independent curvilinear crack paths are observed in the results using the CT-coupling scheme, and the numerical predictions of crack patterns are close to the experimental observations presented in [19].

Acknowledgements

The authors thank US Air Force Office of Scientific Research (Grant FA 9550-10-1-0222) for their generous support of this research. This research was partially supported by Basic Science Research Program through the National Research Foundation of Korea (NRF) funded by the Ministry of Education, Science and Technology (Grant No.: 2012008109).

References

- [1] T.L. Anderson, *Fracture mechanics: Fundamentals and applications*, CRC, 2005.
- [2] G.R. Irwin, *Linear fracture mechanics, fracture transition, and fracture control*, *Engineering Fracture Mechanics* 1 (1968) 241–257.
- [3] G.R. Irwin, D.E. Wit, A summary of fracture mechanics concepts, *Journal of Testing and Evaluation* 11 (1983) 56–65.

- [4] D.S. Dugdale, Yielding of steel sheets containing slits, *Journal of the Mechanics and Physics of Solids* 8 (1960) 100–104.
- [5] G.I. Barenblatt, The mathematical theory of equilibrium cracks in brittle fracture, *Advances in Applied Mechanics* 7 (1962) 55–129.
- [6] G. Ruiz, A. Pandolfi, M. Ortiz, Three-dimensional cohesive modeling of dynamic mixed-mode fracture, *International Journal for Numerical Methods in Engineering* 52 (2001) 97–120.
- [7] J.M. Melenk, I. Babuska, The partition of unity finite element method: basic theory and applications, *Computer Methods in Applied Mechanics and Engineering* 139 (1996) 289–314.
- [8] T. Belytschko, T. Black, Elastic crack growth in finite elements with minimal remeshing, *International Journal for Numerical Methods in Engineering* 45 (1999) 601–620.
- [9] N. Moës, J. Dolbow, T. Belytschko, A finite element method for crack growth without remeshing, *International Journal for Numerical Methods in Engineering* 46 (1999) 131–150.
- [10] J.V. Cox, An extended finite element method with analytical enrichment for cohesive crack modeling, *International Journal for Numerical Methods in Engineering* 78 (2009) 48–83.
- [11] S. Mariani, U. Perego, Extended finite element method for quasi-brittle fracture, *International Journal for Numerical Methods in Engineering* 58 (2003) 103–126.
- [12] G. Meschke, P. Dumstorff, Energy-based modeling of cohesive and cohesionless cracks via X-FEM, *Computer Methods in Applied Mechanics and Engineering* 196 (2007) 2338–2357.
- [13] S. Li, W.K. Liu, Meshfree and particle methods and their applications, *Applied Mechanics Reviews* 55 (2002) 1–34.
- [14] C.L. Rountree, R.K. Kalia, E. Lidorikis, A. Nakano, L.V. Brutzel, P. Vashishta, Atomistic aspects of crack propagation in brittle materials: Multimillion atom molecular dynamics simulations, *Annual Review of Materials Research* 32 (2002) 377–400.
- [15] H. Gao, Y. Huang, F.F. Abraham, Continuum and atomistic studies of intersonic crack propagation, *Journal of the Mechanics and Physics of Solids* 49 (2001) 2113–2132.
- [16] M.J. Buehler, H. Gao, Dynamical fracture instabilities due to local hyperelasticity at crack tips, *Nature* 439 (2006) 307–310.
- [17] G.R. Liu, Y.T. Gu, Coupling of element free galerkin and hybrid boundary element methods using modified variational formulation, *Computational Mechanics* 26 (2000) 166–173.
- [18] J.W. Hong, K.J. Bathe, Coupling and enrichment schemes for finite element and finite sphere discretizations, *Computers & Structures* 83 (2005) 1386–1395.
- [19] M.B. Nooru-Mohamed, E. Schlagen, J.G.M. van Mier, Experimental and numerical study on the behavior of concrete subjected to biaxial tension and shear, *Advanced Cement Based Materials* 1 (1993) 22–37.
- [20] R. De Borst, Some recent developments in computational modelling of concrete fracture, *International Journal of Fracture* 86 (1997) 5–36.
- [21] M. Di Prisco, L. Ferrara, F. Meftah, J. Pamin, R. De Borst, J. Mazars, J. Reynouard, Mixed mode fracture in plain and reinforced concrete: some results on benchmark tests, *International Journal of Fracture* 103 (2000) 127–148.
- [22] P. Pivonka, J. Ožbolt, R. Lackner, H.A. Mang, Comparative studies of 3D-constitutive models for concrete: application to mixed-mode fracture, *International Journal for Numerical Methods in Engineering* 60 (2004) 549–570.
- [23] T.C. Gasser, G.A. Holzapfel, 3D crack propagation in unreinforced concrete: A two-step algorithm for tracking 3D crack paths, *Computer Methods in Applied Mechanics and Engineering* 195 (2006) 5198–5219.
- [24] J.F. Unger, S. Eckardt, C. Konke, Modelling of cohesive crack growth in concrete structures with the extended finite element method, *Computer Methods in Applied Mechanics and Engineering* 196 (2007) 4087–4100.
- [25] B. Patzák, M. Jirásek, Adaptive resolution of localized damage in quasi-brittle materials, *Journal of Engineering Mechanics* 130 (2004) 720–732.
- [26] J. Réthoré, S. Roux, F. Hild, Mixed-mode crack propagation using a hybrid analytical and extended finite element method, *Comptes Rendus Mécanique* 338 (2010) 121–126.
- [27] S.A. Silling, Reformulation of elasticity theory for discontinuities and long-range forces, *Journal of the Mechanics and Physics of Solids* 48 (2000) 175–209.
- [28] S.A. Silling, R.B. Lehoucq, Peridynamic theory of solid mechanics, *Advances in Applied Mechanics* 44 (2010) 73–168.
- [29] S.A. Silling, E. Askari, A meshfree method based on the peridynamic model of solid mechanics, *Computers & Structures* 83 (2005) 1526–1535.
- [30] K. Dayal, K. Bhattacharya, Kinetics of phase transformations in the peridynamic formulation of continuum mechanics, *Journal of the Mechanics and Physics of Solids* 54 (2006) 1811–1842.
- [31] W. Gerstle, N. Sau, S.A. Silling, Peridynamic modeling of concrete structures, *Nuclear Engineering and Design* 237 (2007) 1250–1258.
- [32] P. Demmie, S. Silling, An approach to modeling extreme loading of structures using peridynamics, *Journal of Mechanics of Materials and Structures* 2 (2007) 1921–1945.
- [33] B. Kilic, E. Madenci, Structural stability and failure analysis using peridynamic theory, *International Journal of Non-Linear Mechanics* 44 (2009) 845–854.
- [34] Y.D. Ha, F. Bobaru, Studies of dynamic crack propagation and crack branching with peridynamics, *International Journal of Fracture* 162 (2010) 229–244.
- [35] Y.D. Ha, F. Bobaru, Characteristics of dynamic brittle fracture captured with peridynamics, *Engineering Fracture Mechanics* 78 (2011) 1156–1168.

- [36] B. Kilic, E. Madenci, Prediction of crack paths in a quenched glass plate by using peridynamic theory, *International Journal of Fracture* 156 (2009) 165–177.
- [37] A. Agwai, I. Guven, E. Madenci, Predicting crack initiation and propagation using xfem, czm and peridynamics: A comparative study, in: *Electronic Components and Technology Conference (ECTC)*, 2010 Proceedings 60th, pp. 1178–1185.
- [38] S.A. Silling, O. Weckner, E. Askari, F. Bobaru, Crack nucleation in a peridynamic solid, *International Journal of Fracture* 162 (2010) 219–227.
- [39] E. Askari, J. Xu, S.A. Silling, Peridynamic analysis of damage and failure in composites, in: *44th AIAA Aerospace Sciences Meeting and Exhibit, AIAA2006-88*, pp. 1–12.
- [40] J. Xu, A. Askari, O. Weckner, S.A. Silling, Peridynamic analysis of impact damage in composite laminates, *Journal of Aerospace Engineering* 21 (2008) 187–194.
- [41] B. Kilic, A. Agwai, E. Madenci, Peridynamic theory for progressive damage prediction in center-cracked composite laminates, *Composite Structures* 90 (2009) 141–151.
- [42] W. Hu, Y.D. Ha, F. Bobaru, Modeling dynamic fracture and damage in a fiber-reinforced composite lamina with peridynamics, *International Journal for Multiscale Computational Engineering* 9 (2011) 707–726.
- [43] W. Hu, Y.D. Ha, F. Bobaru, Peridynamic model for dynamic fracture in unidirectional fiber-reinforced composites, *Computer Methods in Applied Mechanics and Engineering* 217 (2012) 247–261.
- [44] S.A. Silling, M. Epton, O. Weckner, J. Xu, E. Askari, Peridynamic states and constitutive modeling, *Journal of Elasticity* 88 (2007) 151–184.
- [45] S.A. Silling, R.B. Lehoucq, Convergence of peridynamics to classical elasticity theory, *Journal of Elasticity* 93 (2008) 13–37.
- [46] T.L. Warren, S.A. Silling, A. Askari, O. Weckner, M.A. Epton, J. Xu, A non-ordinary state-based peridynamic method to model solid material deformation and fracture, *International Journal of Solids and Structures* 46 (2009) 1186–1195.
- [47] D.J. Littlewood, Simulation of dynamic fracture using peridynamics, finite element modeling, and contact, in: *Proceedings of the ASME 2010 International Mechanical Engineering Congress and Exposition (IMECE)*, IMECE2010-40621, pp. 209–217.
- [48] J.T. Foster, S.A. Silling, W.W. Chen, Viscoplasticity using peridynamics, *International Journal for Numerical Methods in Engineering* 81 (2009) 1242–1258.
- [49] J.T. Foster, S.A. Silling, W.W. Chen, An energy based failure criterion for use with peridynamic states, *International Journal for Multiscale Computational Engineering* 9 (2011) 675–687.
- [50] R.W. Macek, S.A. Silling, Peridynamics via finite element analysis, *Finite Elements in Analysis and Design* 43 (2007) 1169–1178.
- [51] P. Lall, S. Shantaram, D. Panchagade, Peridynamic-models using finite elements for shock and vibration reliability of leadfree electronics, in: *Thermal and Thermomechanical Phenomena in Electronic Systems (ITherm)*, 2010 12th IEEE Intersociety Conference, pp. 1–12.
- [52] B. Kilic, E. Madenci, Coupling of peridynamic theory and the finite element method, *Journal of Mechanics of Materials and Structures* 5 (2010) 707–733.
- [53] A. Agwai, I. Guven, E. Madenci, Damage prediction for electronic package drop test using finite element method and peridynamic theory, in: *Electronic Components and Technology Conference (ECTC)*, 2009 Proceedings 59th, pp. 565–569.
- [54] E. Oterkus, Peridynamic theory for modeling three-dimensional damage growth in metallic and composite structures, Ph.D. thesis, The University of Arizona, 2010.
- [55] G. Lubineau, Y. Azdoud, F. Han, C. Rey, A. Askari, A morphing strategy to couple non-local to local continuum mechanics, *Journal of the Mechanics and Physics of Solids* 60 (2012) 1088–1102.
- [56] W. Liu, J.W. Hong, Discretized peridynamics for linear elastic solids, *Computational Mechanics*, <http://dx.doi.org/10.1007/s00466-012-0690-1>.
- [57] W. Liu, J.W. Hong, Discretized peridynamics for brittle and ductile solids, *International Journal for Numerical Methods in Engineering* 89 (2012) 1028–1046.
- [58] M.L. Parks, S.J. Plimpton, R.B. Lehoucq, S.A. Silling, Peridynamics with LAMMPS: A user guide, Technical Report, Technical Report SAND 2008–1035, Sandia National Laboratories, 2008.
- [59] G.T. Mase, R.E. Smelser, G.E. Mase, *Continuum mechanics for engineers*, CRC, 1999.
- [60] K.J. Bathe, *Finite Element Procedures*, Prentice Hall, 2006.
- [61] W. Liu, J.W. Hong, Three-dimensional lamb wave propagation excited by a phased piezoelectric array, *Smart Materials and Structures* 19 (2010) 085002.
- [62] V. Murti, S. Valliappan, Numerical inverse isoparametric mapping in remeshing and nodal quantity contouring, *Computers & Structures* 22 (1986) 1011–1021.
- [63] V. Murti, Y. Wang, S. Valliappan, Numerical inverse isoparametric mapping in 3D FEM, *Computers & Structures* 29 (1988) 611–622.
- [64] C. Chinnaswamy, B. Amadei, T.H. Illangasekare, A new method for finite element transitional mesh generation, *International Journal For Numerical Methods in Engineering* 31 (1991) 1253–1270.
- [65] J.O. Hallquist, *LS-DYNA theory manual*, Livermore Software Technology Corporation, Livermore, California, 2006.
- [66] P. Wriggers, *Computational Contact Mechanics*, Springer, 2006.
- [67] H. Moslemi, A.R. Khoei, 3D adaptive finite element modeling of non-planar curved crack growth using the weighted superconvergent patch recovery method, *Engineering Fracture Mechanics* 76 (2009) 1703–1728.